

2020-01-01

Photovoltage Enhancement for Stable Perovskite Solar Cells with a Temperature-Controlled Grain Growth Technique

Luis Eduardo Valerio
University of Texas at El Paso

Follow this and additional works at: https://scholarworks.utep.edu/open_etd



Part of the [Electrical and Electronics Commons](#), [Oil, Gas, and Energy Commons](#), and the [Sustainability Commons](#)

Recommended Citation

Valerio, Luis Eduardo, "Photovoltage Enhancement for Stable Perovskite Solar Cells with a Temperature-Controlled Grain Growth Technique" (2020). *Open Access Theses & Dissertations*. 3054.
https://scholarworks.utep.edu/open_etd/3054

This is brought to you for free and open access by ScholarWorks@UTEP. It has been accepted for inclusion in Open Access Theses & Dissertations by an authorized administrator of ScholarWorks@UTEP. For more information, please contact lweber@utep.edu.

PHOTOVOLTAGE ENHANCEMENT FOR STABLE PEROVSKITE SOLAR CELLS WITH
A TEMPERATURE-CONTROLLED GRAIN GROWTH TECHNIQUE

LUIS EDUARDO VALERIO FRIAS

Master's Program in Electrical Engineering

APPROVED:

Deidra Hodges, Ph.D., Chair

David Zubia, Ph.D.

Felicia Manciu, Ph.D.

Stephen L. Crites, Jr., Ph.D.
Dean of the Graduate School

Copyright ©

by

Luis Eduardo Valerio Frias

2020

Dedication

To God, my family, friends and fellow lab mates within the Thin Film Photovoltaics Lab

PHOTOVOLTAGE ENHANCEMENT FOR STABLE PEROVSKITE SOLAR CELLS WITH
A TEMPERATURE-CONTROLLED GRAIN GROWTH TECHNIQUE

by

LUIS EDUARDO VALERIO FRIAS, BSEE

THESIS

Presented to the Faculty of the Graduate School of

The University of Texas at El Paso

in Partial Fulfillment

of the Requirements

for the Degree of

MASTER OF SCIENCE

Department of Electrical and Computer Engineering

THE UNIVERSITY OF TEXAS AT EL PASO

May 2020

Acknowledgements

Thank you, Dr. Deidra Hodges, for giving me my first opportunity to show what I am capable of achieving. Thanks to the Thin Film Photovoltaics Lab Members: Angel De La Rosa and Christian Enriquez. Also, thanks to Brookhaven National Laboratory, the National Renewable Energy Lab, and the UTEP Materials and Metallurgy Department faculty and staff.

Abstract

By performing strong characterizations methods, one can begin to fully understand the chemistry and composition behind a great performing perovskite solar cell. Understanding how the interaction between layers inside a solar cell is driven by the temperature and overall environment is a key element to improve the fabrication process and overall efficiency of such cells. This thesis will present a study of the hybrid organic-inorganic, mixed-cation, mixed-halide, temperature and thickness-controlled perovskite solar cell. A constant power conversion efficiency (PCE) ranging between 15-17% and an open circuit voltage V_{oc} above 1.05 V for a wide-band gap perovskite cell is presented.

Table of Contents

Dedication.....	iii
Acknowledgements.....	v
Abstract.....	vi
Table of Contents.....	vii
List of Tables.....	viii
List of Figures.....	ix
Chapter 1: Introduction.....	1
Chapter 2: Theory of Perovskite Material.....	4
2.1: Background.....	4
2.2: Literature Review and Previous Results.....	8
Chapter 3: Model Methodology and Development.....	21
3.1: Mixed-cation, mixed-halide, SnO ₂ -based perovskite device.....	21
3.2: Device fabrication.....	22
Chapter 4: Results, Characterization, and Discussion.....	24
4.1: X-ray Photoelectron Spectroscopy and Ultraviolet Photoelectron Spectroscopy.....	24
4.2: Photoluminescence spectroscopy and lifetime.....	27
4.3: SEM and AFM.....	28
4.4: J-V and EQE Measurements.....	32
Chapter 5: Future Work and Conclusion.....	37
5.1: Future Work on Guanidinium Bromide for secondary grain growth.....	37
5.2: Conclusion.....	39
References.....	40

Vita 44

List of Tables

Table 2.1: Summary of Perovskite-Based Cells ¹⁶	5
Table 4.1: Summary of Results for Perovskite A cells	35

List of Figures

Figure 2.1 DSSCs solar cell schematic ¹⁵	5
Figure 2.2 Nanocomposite embodiment of a perovskite solar cell ⁶	6
Figure 2.3 ABX ₃ stoichiometry of perovskite.....	7
Figure 2.4 Shockley-Queisser model for energies greater than bandgap	8
Figure 2.5 Spin-coating process.....	10
Figure 2.6 CBD process with post-annealing at 180 °C ²²	11
Figure 2.7 PVD process	11
Figure 2.8 Evolution of diffraction peaks corresponding to PbI ₂ and MAPbI ₃ ²⁷	14
Figure 2.9 Atomic % documentation after 25 and 1000 hours ²⁶	14
Figure 2.10 Bandgap dependence of pseudo-cubic lattice constant a _o ³⁸	17
Figure 2.11 Chemical structure of spiro-OMeTAD and spirobifluorine ³	18
Figure 2.12: Carrier mobility and annealing time relationship ⁴⁰	19
Figure 3.1: n-i-p device structure for perovskite solar cells.	21
Figure 3.2: Masking pattern used for Ag evaporated back contacts.....	23
Figure 4.1: XPS survey spectra of the Perovskite A documented after 500 hours showing a small oxygen and lead peak, indicator of good stability.	25
Figure 4.2: XPS survey spectra of the Perovskite B documented after 500 hours showing a big lead peak, indicator of lead migration due to oxidation of perovskite layer.....	26
Figure 4.3: UPS spectra showing the work function and valence band for both Perovskite A and Perovskite B.....	26
Figure 4.4: PL spectra showing a wavelength of 1.59 eV for Perovskite A and 1.74 eV for Perovskite B.....	27
Figure 4.5: PL decay and lifetime for Perovskite A with a lifetime of 274.69 ns and Perovskite B with a lifetime of 17.99 ns.	28
Figure 4.6: SEM of Perovskite A-based device showing a cross section of the layers in the device structure.....	30
Figure 4.7: Top view SEM image of Perovskite A film showing the average crystal size close to 100 nm.	31
Figure 4.8: AFM measurement of Perovskite A showing the roughness and average grain size close to ~147 nm. This compares with the 100 nm shown in the SEM data.	32
Figure 4.9: Thickness and topography of Perovskite A showing a thickness close to 400 nm. ...	32
Figure 4.10: Perovskite A and Perovskite B J-V curves annealed at 100 °C for 1 hour.	35
Figure 4.11: Perovskite A and Perovskite B EQE curves annealed at 100 °C for 1 hour.	35
Figure 5.1 SEM images of the control and SSG-G films showing a reduction of PbI _{1.50} Br _{0.50} grains due to the secondary grain growth. ⁵⁷	38

Chapter 1: Introduction

There is an urge inside the scientific community of improving the performance and costs of environmental-friendly energy sources able to compete with traditional fossil fuel-based generation systems. Several types of these clean energies technologies have emerged in recent history. Such examples include wind energy with exceptional efficiencies ranging between 45-60%¹, with the only main disadvantage of high costs and lack of infrastructure. Another example includes thermoelectric-based systems capable of converting heat flux into electrical energy. These systems have just been able to achieve low conversion efficiencies between 5-10%². Still, it is known that photovoltaics has established themselves as the main choice of renewable energy technology due to its promising efficiencies and low costs. Photovoltaics is the conversion of energy in form of light into electrical energy. Silicon solar cells have become the main type of solar cells generating photovoltaic energy. In recent years, their efficiency has already achieved standard average efficiencies of 26%³. Theoretically, silicon solar cells can achieve a maximum efficiency of 29%, making the search of new photovoltaic technologies capable of achieving greater efficiencies a very interesting topic to research. Such research has been focusing on detecting and solving some of the deficiencies that traditional silicon solar cells could present. One example, is the absence of energy collection at higher energy levels than the theoretical band gap of silicon (~1.12 eV). As a result, a material capable of absorbing light at different band gaps, or with bandgap tuning properties is desirable. This thesis presents the use of perovskite solar cells (PSCs), which have become an important solar energy technology in the last years, as studied by our research team^{4,5}. Its power conversion efficiency (PCE) has improved from its initial average values ranging 5-10%^{6,7} to record values of 25.2%^{3,8,9}, and tandem cells efficiencies surpassing 29%¹⁰⁻¹², in where perovskite solar cells with different band gaps are stacked to absorb a wider

range of the light spectrum. This thesis in particular will present a stable and high-efficiency mixed-cation, mixed-halide, tin oxide (SnO_2) based perovskite devices. These devices have been able to achieve power conversion efficiencies ranging between 15%-17% thanks to an optimization of all the layers' thicknesses through a correct deposition process, chemical ratio, temperature control, and manufacturing processes in general. Also, these devices have achieved a stable and constant overall performance due to the correct temperature control during all the fabrication process.

Chapter 2 will introduce the history, theory, and chemistry behind the perovskite material. Understanding its ABX_3 stoichiometry, in where A corresponds to a monovalent organic A-site cation, B to a divalent B-site cation as a metal, and a X-site anion as halides, is crucial to understand its properties, its bandgap tuning capability, how this impacts the Shockley-Queisser (SQ) model, and how changing the ratios of the chemicals in the perovskite changes its properties, impacting its performance, stability, and overall efficiency. Chapter 2 will also go over previous remarkable work, where research groups have tried all different type of approaches as changing the cations or halides in the stoichiometry. This chapter will also present different types of deposition as spin coating, chemical bath deposition (CBD), thermal evaporation, or dip coating.

Chapter 3 will present the model utilized for this thesis in where the research group utilizes a mixed-cation, formamidinium (FA), cesium (Cs), mixed-halide, iodine (I), bromine (Br) perovskite recipe. It will present the fabrication process with specific temperatures, times, and controlled thickness.

Chapter 4 will present the different characterization methods utilized to analyze the composition and overall performance of these devices. X-ray photoelectron spectroscopy (XPS) provides chemical composition of the material at the surface. Ultraviolet photoelectron

spectroscopy (UPS) measures the work function and bandgap. Photoluminescence spectroscopy (PL) and lifetime analysis shows the bandgap at which light is absorbed in the material and the carriers' lifetime. Scanning electron microscope (SEM) and atomic force microscopy (AFM) provide a map of the surface and an approximate grain size. Current density-voltage measurements utilize a solar simulator to provide key information, as current density (J_{sc}), open-circuit voltage (V_{oc}), shunt resistance (R_{SH}), series resistance (R_s), and power conversion efficiency (PCE). Finally, the external quantum efficiency (EQE) shows the ratio of number of carriers collected to number of photons at a specific wavelength on a device.

Finally, chapter 4 presents a conclusion, and thoughts about work that can be potentially done in the future. This future work research will be based on a similar process, with the difference of the addition of guanidium bromide as an additive to produce a secondary perovskite grain process to achieve higher open-circuit voltages and power conversion efficiencies.

Chapter 2: Theory of Perovskite Material

2.1: BACKGROUND

In 1839, perovskite as a mineral based on CaTiO_3 , was discovered by Gustav Rose in Russia. It was later named perovskite after Lev Aleksevich von Perovski, a Russian scientist. Perovskite is the nomenclature given to any material with a similar crystal structure as calcium titanate, or as it will be seen through the paper, an ABX_3 stoichiometry. These materials were commonly fabricated by using solid-state synthesis in where the elements present in the material are synthesized at high temperatures. Later, it was discovered that these materials could be fabricated using precursor salts, making its fabrication and potential applications much easier.^{6,7,13} It was until the 20th century when the scientific community started to explore the applications of this material due to its magnetic and optical/electronic properties¹⁴. The experiments from research groups lead by Mitzi and Era were focusing on these organometal materials which presented potential uses in transistors and light-emitting diodes (LED)¹⁴.

In the last ten years research has focused on the utilization of perovskite as an active absorber layer for solar cells. These perovskite-based solar cells emerged due to the past research in dye-sensitized solar cells (DSSCs). DSSCs are devices made up of a mesoporous n-type TiO_2 , a redox-active electrolyte and a light-absorbing dye¹⁵. The structure of a DSSCs consists of a layer of the porous TiO_2 “coated” with the light-absorbing dye. This dye, as its name states, is responsible for the absorption of the incident light to then react with the electrolyte. Brian E. Hardin, and Henry J. Snaith presented the structure seen in Figure 2.1 for a DSSCs device¹⁵. They also stated that the thickness limit of the absorber layer was the main drawback of these type of devices. DSSCs devices with the traditional TiO_2 layer needed to be at least 10 μm to achieve an acceptable absorbance, but due to its chemical composition, the maximum thickness they could

achieve was close to 2 μm . The research shifted towards the fabrication of DSSCs devices using inorganic absorbers, or thin semiconductor absorber layers. The optoelectronic properties of organometals materials such as perovskites made them the strongest candidate to fabricate new type of DSSCs devices. T. Miyasaka and his research team presented the first perovskite-sensitized solar cell¹⁶. In their works, they employed $\text{CH}_3\text{NH}_3\text{PbI}_3$ or $\text{CH}_3\text{NH}_3\text{PbBr}_3$ as their perovskite material along with a triiodide redox couple. A summary of the results achieved with these first perovskite-based devices can be seen in Table 1 retrieved from T. Miyasaka publication¹⁶.

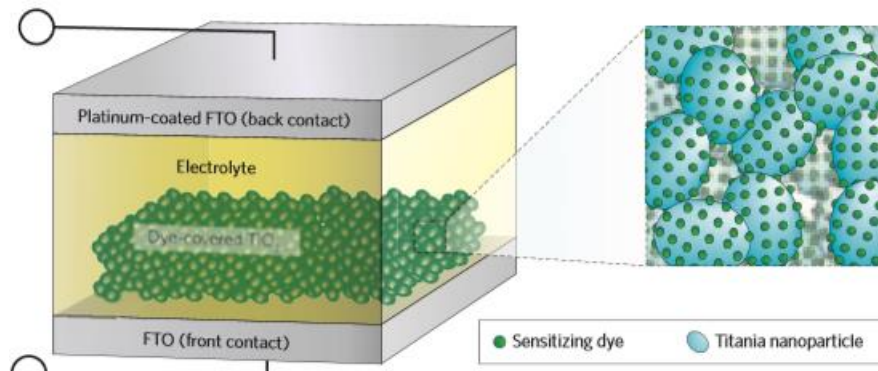


Figure 2.1 DSSCs solar cell schematic¹⁵

Table 2.1: Summary of Perovskite-Based Cells¹⁶

perovskite sensitizer on TiO_2	J_{sc} (mA/cm^2)	V_{oc} (V)	FF	η (%)
$\text{CH}_3\text{NH}_3\text{PbBr}_3$	5.57	0.96	0.59	3.13
$\text{CH}_3\text{NH}_3\text{PbI}_3$	11.0	0.61	0.57	3.81

The technology was emerging, and years later N.G. Park and co-workers were able to achieve a 6.5% efficiency utilizing also $\text{CH}_3\text{NH}_3\text{PbI}_3$ as their perovskite and TiO_2 as their electron transport layer. The difference was the use of this perovskite as a liquid electrolyte material¹⁷. The problem with this approach, and previous experiments, was the quick degradation of the absorber presented by decomposing into the electrolyte just minutes after being applied. The solution came later by adding a hole conductor layer, or as it will be later known a hole transport layer, giving as

a result the early n-i-p configurations for perovskite solar cell devices⁶⁻⁹. This also improved the stability of the devices by stopping the use of liquid solvents. In this configuration, the TiO₂ and the hole transport layer work as selective contacts in where the electrons are absorbed by TiO₂ and the holes by the hole transport layer further discussed in following sections. Also, the perovskite layer is responsible for the extraction of carriers and the transportation of both electrons and holes⁶⁻⁹. M. Graetzel presents in his perovskite commentary Figure 2.2 to illustrate the nanocomposite embodiment of a perovskite solar cell with the TiO₂ in the perovskite and the hole transport layer to form the earlier models of a n-i-p device structure⁶.

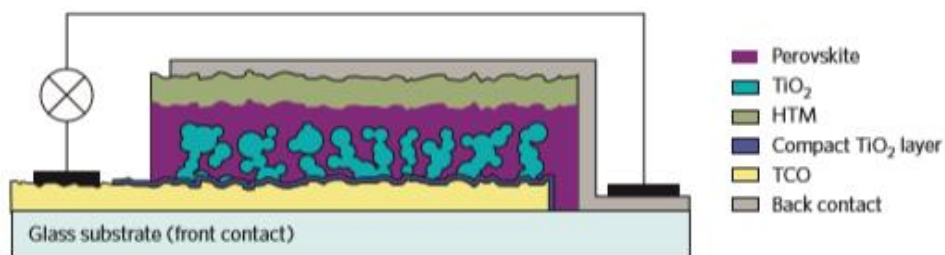


Figure 2.2 Nanocomposite embodiment of a perovskite solar cell⁶

In the last years, research groups lead by Michael Graetzel and Henry Snaith started to provide power conversion efficiencies surpassing the 3-5%^{6,7} efficiency. This was done by focusing on the metal halide perovskite configuration and stoichiometry.

The hybrid metal-halide perovskite utilized in current perovskite solar cells (PSCs) present an ABX₃ stoichiometry, in where A represents a monovalent A-site cation, B a divalent B-cation of metal, and X a X-site anion for halides. Some examples for the A-site cation include methylammonium (MA), formamidinium (FA), and cesium (Cs). Lead (Pb) and tin (Sn) are commonly used for the divalent B-site cation of metal, and bromine (Br), chlorine (Cl), or iodine

(I)¹⁴ for the halides. Figure 2.3 illustrates the crystal structure for the ABX₃ stoichiometry of the perovskite.

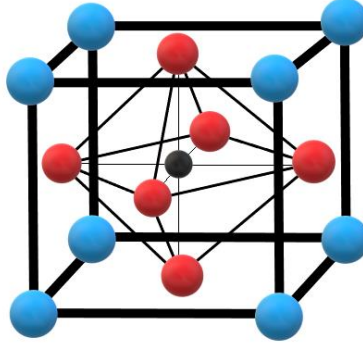


Figure 2.3 ABX₃ stoichiometry of perovskite

This cubic perovskite structure depends on the Goldschmidt tolerance factor to measure the fit of the A-site cation and the B-site octahedron frame¹⁸. The Goldschmidt tolerance factor also provides indications for stability of the crystal, which for perovskite is crucial to understand its stability against environment and humidity. The Goldschmidt tolerance factor is mathematically defined by Equation (2.1).

$$t = \frac{r_A + r_X}{\sqrt{2}(r_B + r_X)} \quad \text{Equation (2.1)}$$

Here r_A , r_B , and r_X are the radii of the A-site cation, the B-site cation, and the X-site anion. The A-site cation achieves a perfect fit with the B-site frame when the tolerance factor, $t = 1$. In reality, most of the crystal structures are not capable of achieving that tolerance factor. If the tolerance factor is $t < 1$ the A-site cation is small to fit correctly in the B-site frame, causing octahedral tilting, which directly affects the optical absorption and emission properties of the perovskite¹⁹. A tolerance factor $t > 1$, means that the A-site cation now is too big for the B-site cation frame, causing an electronically driven distortion²⁰.

The Shockley-Queisser (SQ) model, shown in Figure 2.4., states that photons striking an ideal material with an energy value higher than the band gap of such material will produce free

electron and holes. These carriers are then absorbed by the contacts, creating electron-hole pairs, which eventually produce electrical current¹³. This means that in traditional solar cells there is a limitation of how much energy can be absorbed from the light spectrum. If the bandgap is too high, only photons with higher energies will be able to produce the electron hole pairs, producing less current. However, if the bandgap is low the excess energy coming from the light will be lost in form of heat. This is the reason of why research is now focusing on perovskite as a material capable of tuning its bandgap.

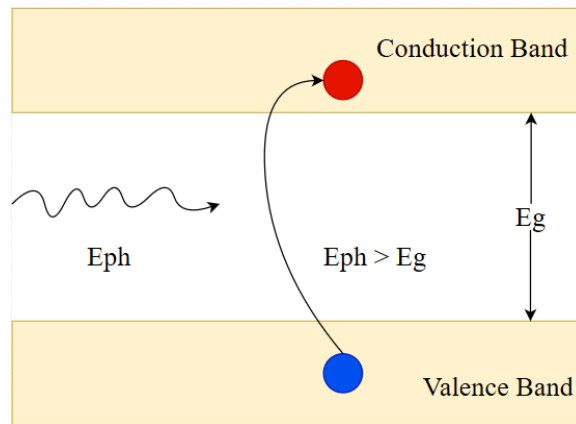


Figure 2.4 Shockley-Queisser model for energies greater than bandgap

2.2: LITERATURE REVIEW AND PREVIOUS RESULTS

Being a popular material nowadays, many approaches have been used to achieve higher efficiencies and overall performances of perovskite solar cells. As mentioned before, the power conversion efficiencies have increased substantially from its initial values ranging between 5-10%^{6,7} to a world record efficiency of 25.2%^{3,8,9}, and tandem cells average efficiencies of 29%¹⁰⁻¹².

Another property that makes perovskite solar cells interesting is its low-cost fabrication and reproducible results²¹. It is known that silicon solar cells are traditionally fabricated with etching and lithography process, which must be performed in a clean room of at least Class 10,

which corresponds to the allowable number of particles per cubic foot of air. On the contrary, perovskite solar cells can be produced utilizing solution and vapor low temperature techniques, such as chemical bath deposition (CBD), spin coating, physical vapor deposition, and dip coating²².

The spin coating process is the most common process for lab-scale fabrication of small perovskite solar devices. In this process a device is placed in a spin coater under vacuum, then the solution is placed in the center of the substrate. This can be done while the substrate is spinning (active deposition) or without spinning (passive deposition). The advantage of this process is the creation of uniform thin layers by spreading it with the rotation movement. This movement can be done at different revolutions per minute and different times to create different thicknesses. Perovskite solar devices best results are still on a smaller scale, making spin coating the most proficient process to control film thickness²³. Figure 2.5 shows a diagram of a spin coating process. As discussed, one of the main challenges perovskite solar devices still have is its scalability for commercialization and mass production. Performing spin coating on larger scale devices increases the presence of pinholes on the surface. Pin holes are defects that damage the device by causing shorts circuits between the electrodes of a thin film and other layers of the device. These pinholes are thickness dependent caused by air bubbles produced during the solution dispensing, by particles due to unclean dispense tips in such solution, or by particles already existing in the surface prior to the dispense. It is more difficult to control these factors at larger scale devices, increasing the number of pinholes. This is the reason, other deposition methods are added and combined to the fabrication process to create more stable devices.

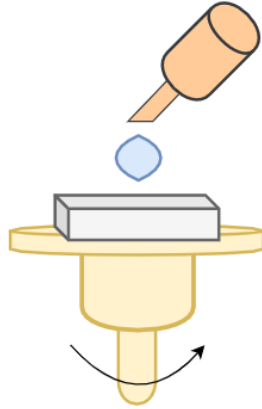


Figure 2.5 Spin-coating process

Chemical bath deposition (CBD) is a process usually used in a two-step deposition for oxide films. CBD is attractive as a hot plate, inexpensive chemicals, and petri dish is only needed. CBD is commonly used to deposit layers in top of insoluble surfaces. In this thesis the CBD is used to grow the SnO_2 layer. In this process the substrate is submerged in the liquid solution of the layer that needs to be grown. The reaction occurs spontaneously at the liquid phase of the dissolved precursors²⁴. The devices are then placed in a hot plate at low temperatures (below 100 °C) for long periods of time. The low temperatures prevent the corrosion and oxidation of metallic substrates²⁴. In this case, the metallic substrate is the FTO and the SnO_2 layer beneath the CBD grown SnO_2 layer. The CBD provides at the end a uniform layer, with blocking layers with high selectivity and stability, preventing pin holes and leaks from bottom layers²². E. Anaraki et al present in their paper Figure 2.6 a chemical bath deposition process diagram with a post-annealing process to increase blocking capabilities²⁵.

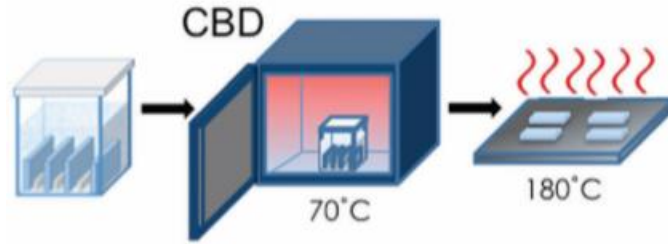


Figure 2.6 CBD process with post-annealing at 180 °C²²

Physical vapor deposition (PVD) is the process in which a liquid or solid material is vaporized into atoms to then be transported through vacuum into the substrate in the top, in where it condenses forming a thin film layer²⁵. PVD is usually used to form thin (nm scale) layers on a substrate. In a vacuum deposition, the material travels upward with almost no collisions by being in vacuum, preventing contamination. The main advantage of this process is the ability of producing uniform and reproducible layers due to the vacuum environment, being the cost of the materials and the equipment its main challenge. Figure 2.7 illustrate a common PVD process in where the evaporated atoms travel through vacuum upward into the target.

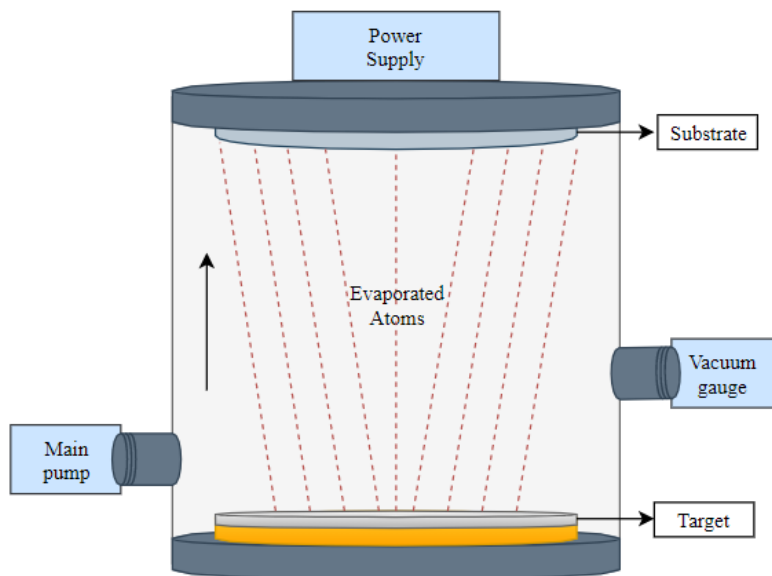


Figure 2.7 PVD process

Still, the limiting factor that prevents commercialization of perovskite solar cells is its tendency to degrade after being exposed to the environment and humidity. In the ABX_3 stoichiometry, methylammonium (MA or CH_3NH_3) is traditionally used for the A-cation, being methylammonium lead triiodide ($MAPbI_3$) the most traditional perovskite mixture. Research has concluded that MA has a strong moisture sensitivity making it decompose into PbI_2 after being exposed for a short time to the environment, making the perovskite film reverse into its precursor state^{26,27}, limiting open-circuit voltage^{28,30}. This is caused by the hygroscopic nature of the alkylammonium cation present in the unit cell²⁸. This hysteresis could be caused by the photo-induced structural change of the material. The decomposition of MA into PbI_2 occurs just after any annealing process. Light and oxygen in the environment are the main causes of the degradation, meaning that the decomposition starts at the surface of the film in the grain boundaries. At first, the PbI_2 produced actually enhances the lifetime of chargers as it produces a passivation process that reduce the recombination traps at the grain boundaries, but this decomposition continues until it falls into its precursor state²⁷. This is proven and illustrated by V. Kheraj and the research team of the S.V. National Institute of Technology in Surat, India in Figure 2.8 showing an X-ray diffraction spectrum in where it can be seen how the diffraction peaks of PbI_2 and $MAPbI_3$ evolve rapidly with time²⁷. XRD is used to determine the molecular structure of a crystal by shooting an X-ray beam into the crystal to then get diffracted into many directions. Every direction has a specific angle and intensity, and these angles and intensities correspond to a specific material inside the crystal structure. In Figure 2.8 a small peak at $2\theta = 14^\circ$ is seen 0.3 hours after being exposed to the environment and a strong peak at 12.6° . The 14° peak corresponds to $MAPbI_3$ and the 12.6° to the PbI_2 phase. The following surveys corresponds to bigger exposition times to environment in where the PbI_2 keeps increasing while the $MAPbI_3$ keeps getting smaller.

This indicates the degradation of MAPbI_3 into PbI_2 which brings additional implications as migration of layers beneath the perovskite thin film in the device structure. As stated, the typical device structure of a perovskite solar cell is composed by FTO/ITO, $\text{SnO}_2/\text{TiO}_2$, the perovskite layer, hole transport layer, and the back-metal contact. By using x-ray photoelectron spectroscopy (XPS), which will be further discussed in the results section, one can look at the atomic % of each element present in the surface of a film. In Figure 2.9, Z. Ahmad et al present a graph comparing the atomic % of elements after 25 and 1000 hours. They used ITO, TiO_2 , and MAPbI_3 as their front contact, hole transport, and perovskite layer respectively²⁶. The presence of carbon, nitrogen, lead, and iodine is expected due to the chemical composition of MAPbI_3 , but after some hours the presence of indium, tin, and titanium increases substantially, meaning a leak or migration of this elements occurred from the electron transport layer, and the front contact into the perovskite layer causing chemical instabilities in the absorber layer.

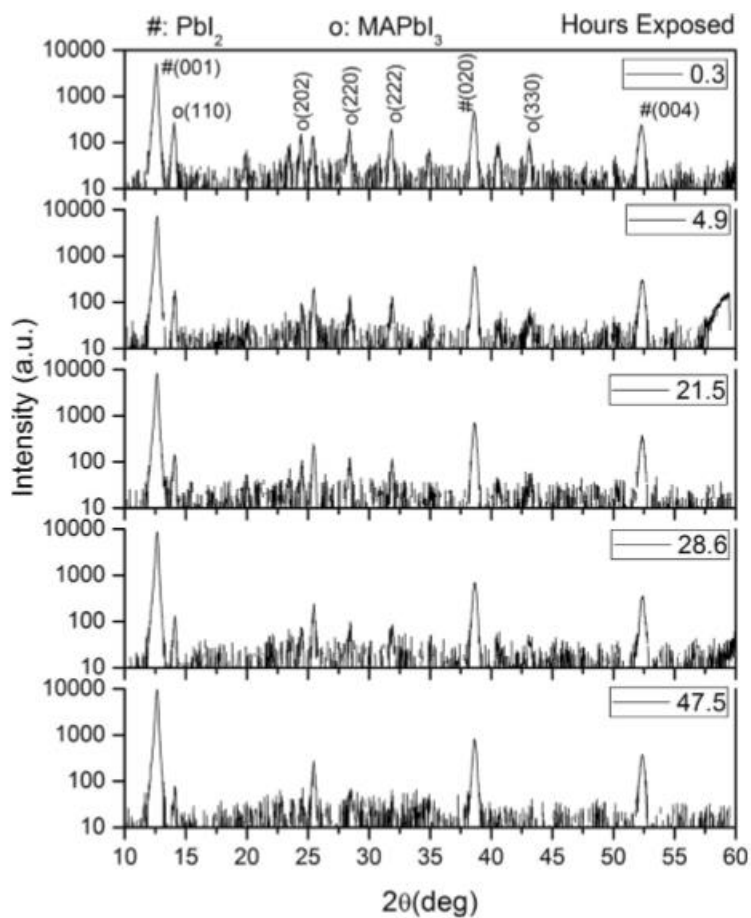


Figure 2.8 Evolution of diffraction peaks corresponding to PbI_2 and MAPbI_3 ²⁷

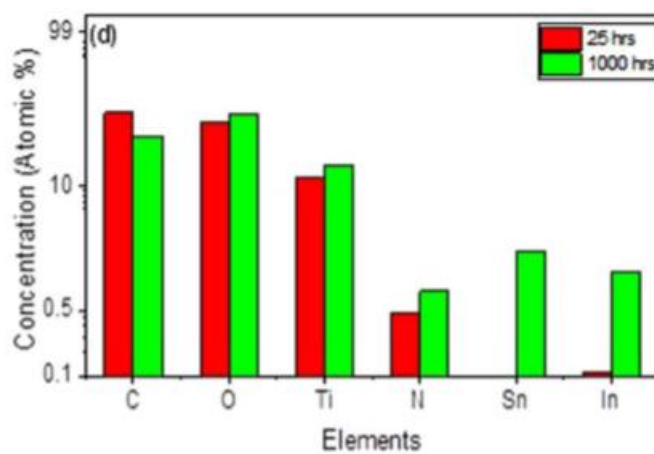


Figure 2.9 Atomic % documentation after 25 and 1000 hours²⁶

Steps have been taken to eventually remove MA from the mixture and instead utilize mixed-cations for the A-site cation. The research presented in this thesis will look into the use of

a mixture of formamidinium (FA) and cesium (Cs), capable of achieving efficiencies above 21%^{29,30}. Using FAPbI₃ instead of MAPbI₃ has proven to provide a reduced band gap improving light harvesting³⁰. However, at room temperature this compound tends to have structural problems and crystallizes into a yellow phase, increasing the sensitivity against temperature and humidity. At the same time, using CsPbI₃ provides a band gap of 1.73 eV with good emissive properties, but at room temperature it also crystallizes into a yellow phase. The proposed solution is to take the benefits of both Cs and FA and mix them as the A-site cation. From literature review, it is known that this mixture improves stability against temperature and humidity, while also enhancing absorption by increasing crystal size due to entropic stabilization, which reduces yellow phase impurities^{30,31}. The Cs/Fa cation has also been proven to improve the Goldschmidt tolerance factor, making the crystal more stable. Also, the FA-Cs mixed cation helps the FA-halide interaction (halide is the X-site anion in the mixture), which improves open-circuit voltage^{32,33} by reducing the number of available traps near the surface³⁴. In summary Cs helps FA to move towards a black perovskite phase with better and faster crystallization rate compared to MA-perovskite based cells.

Changing the A-site cation is only one approach to improve performance. The X-site anion can also be modified. Early perovskite mixtures were made of triiodide as its X-site anion. Being by itself meant a small bandgap for the whole mixture, meaning by Shockley Queisser model that any high energy photon will cause the electron-hole pair generation, but the majority of the energy will be lost in the form of heat³⁵. This opens the door to the utilization of mixed halides for the X-site anion. In concrete, this thesis will focus on the use of a mixture of iodine and bromine. Using a mixture of halides is what gives perovskite the ability to tune its bandgaps as the smaller halide reduces the polarization of the perovskite, which eventually improves absorption and increases the bandgap of the mixture^{36,37,38}. This bandgap tuning causes different crystal colors and absorption

coefficients meaning that the bandgap is directly correlated to the anion radius of the halides and the pseudo-cubic lattice parameter a_0 . For example, a perovskite compound with a mixed iodine-bromine halide mixture with high concentration of bromine will present a cubic crystal structure while a low bromine concentration adopts a tetragonal crystal structure³⁸. Different crystal structures are what changes the band gap as the interatomic distance is changed. A smaller lattice parameter decreases the interatomic distance which increases the binding forces between valence electrons, meaning more energy is required to excite them from the valence band into the conduction band. The minimum energy required to produce this excitation equal to the difference between the conduction band energy minimum, E_c and the valence band energy maximum, E_v ($E_c - E_v$) is called the bandgap energy. The band gap energy is inversely proportional to the associated effective mass, which is proportional to the lattice parameter^{36,37,38}. This is reflected in Figure 2.10 from E. Unger paper in where the research team compares different perovskite mixtures with different halides and anions in general³⁸ and Equation (2.2). A fitted curve is shown to show how the absorption onset (band gap) is inversely proportional to the pseudo-cubic lattice constant a_0 .

$$E_g = \frac{\hbar^2 k^2}{2m^*} \quad \text{Equation (2.2)}$$

With the mixture of iodine and bromine, the bandgap can be tuned to values between 1.5 and 2.3 eV^{33,36,37,39}. Devices close to 1.6 eV tend to approach the theoretical efficiency limit of single junction device, but still high band gap devices (> 1.7 eV) tend still to present high efficiencies. At higher band gaps than 2.3 eV devices start to present ionic inhomogeneity, which makes the crystal and the material in general very unstable³⁸. Combining low and high band gap devices gives the opportunity to build a device capable of approaching the optimum band gap while still absorbing at other band gaps of the light spectrum. In summary, by changing the ratios of the two halides, one can easily tune the bandgap to a desirable energy. Many steps have been

taken in research to improve the perovskite active layer, but still there have been work in the improvement of the other layers in a perovskite solar cell.

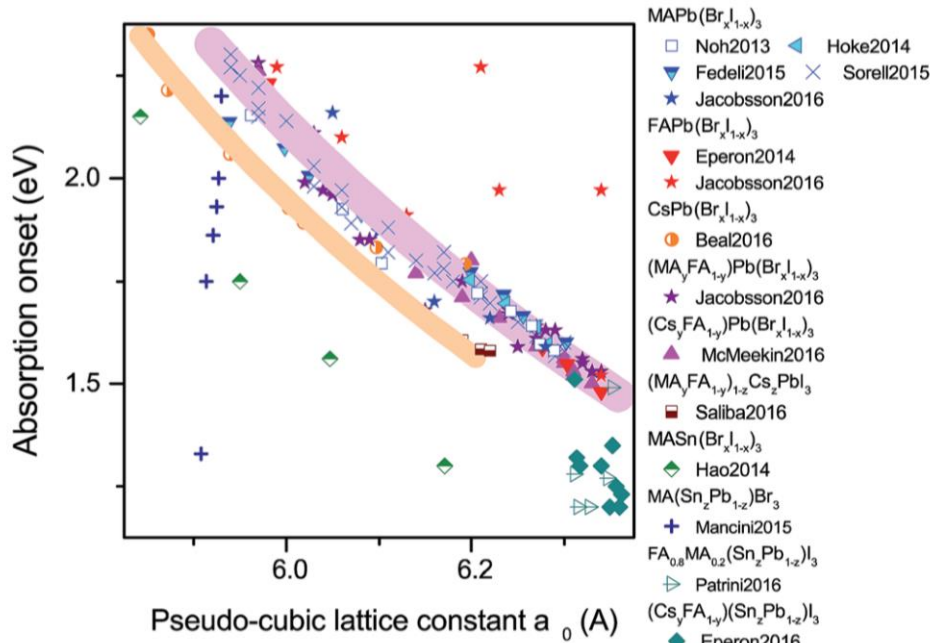


Figure 2.10 Bandgap dependence of pseudo-cubic lattice constant a_0 ³⁸

Solar cells are usually constituted by a front contact, an electron transport layer (ETL) (n-channel), an active absorber layer, a hole transport layer (HTL) (p-channel), and a metal back contact. Improvements can also be done on these other layers, especially in the electron and hole transport layers to prevent recombination at the traps between the active perovskite layer and these two transport layers. Several approaches have been done in the literature review. The use of spirobifluorine has been proposed as the hole transport layer instead of the commonly used spiro-OMeTAD³. In this paper, N. Jeon et al sustain that the use of spirobifluorine provides a higher driving force for hole injection. In general, the quality, the physical and optoelectronic properties of the hole transport layer depend on the conjugated structure of its core. Spirobifluorine provides a stronger core structure with a peripheral group molecular structure while spiro-OMeTAD shows a p-anisole structure. Both structures are illustrated in N.Jeon paper and in Figure 2.11³. Spiro-

OMeTAD shows also a high degradation against thermal stress. On the other hand, spirobifluorine, due to its molecular structure, provides a highest occupied molecular orbital (HOMO) energy level matched to perovskite and a higher glass transition temperature (T_g)³. This temperature is the transition of the material from a “glassy” crystalline structure into a more viscous state. A higher glass transition temperature means a stronger crystallization state, making it more stable against higher temperatures and the environment in general.

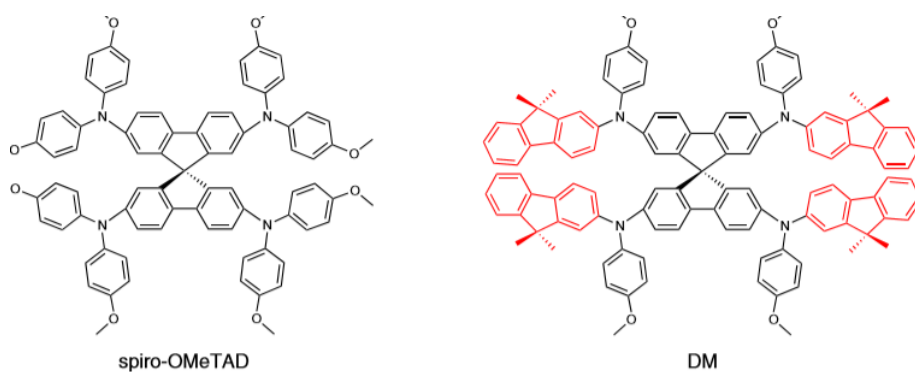


Figure 2.11 Chemical structure of spiro-OMeTAD and spirobifluorine³

Changing the temperatures at the annealing process plays an important role to improve grain size of the perovskite film.⁴⁰ Increasing the temperature slows down the crystallization process of the perovskite meaning larger crystal domains are created. A longer annealing process gives opportunity to unreacted materials to consume and decrease the grain boundaries. This changes the topography of the surface from a rough and irregular surface into a smoother one. The bigger grains increase the mobility of the carriers by decreasing the recombination traps caused by the grain boundaries. At the same time, one must be cautious as a prolonged annealing process (~100 min or longer), or performing it at very high temperatures actually decreases the mobility of the carriers making the device unusable. A. Zeidell et al present in their paper Figure 2.12 in where the relationship between annealing time and mobility is illustrated. From this graph it can

be seen that the optimum time for higher carrier mobility is around 60 to 80 minutes, being the 80 minutes the time that showed the highest mobility in their research⁴⁰. Also, at 100 min as they discussed in their paper, the carrier mobility starts to decrease. Still there must be more research for the cases in where the temperature is increased but the time decreased or a decrease in time but an increase of temperature.

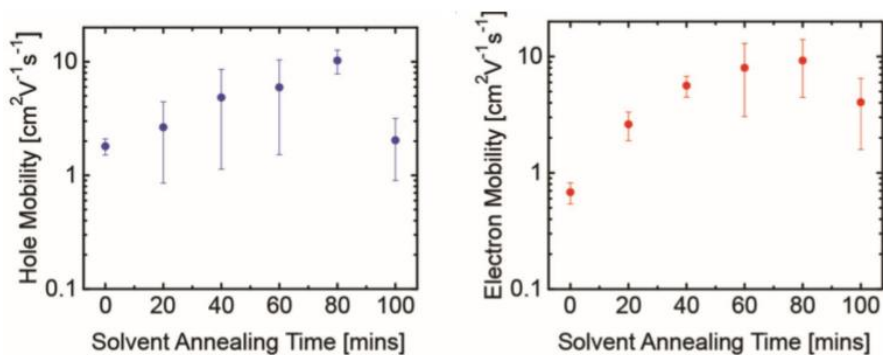


Figure 2.12: Carrier mobility and annealing time relationship⁴⁰

This thesis will present the use of tin oxide (SnO₂) as the electron transport layer. Tin oxide enhances the band alignment between the active perovskite layer and the ETL, meaning that tin oxide presents a higher carrier mobility^{41,42}. These properties have been utilized to obtain high efficiencies surrounding 20%^{22,43}. Other materials have been utilized for the electron transport layer. Zinc oxide has been proposed, but its reactive relationship with the perovskite layer has affected its efficiency and stability after being exposed to the environment⁴⁴. In early cells, titanium oxide was the main option for the ETL, but it has a much smaller carrier mobility compared to tin oxide, and also degrades at a faster rate⁴⁴. Other approaches presented in literature is the doping of the electron transport layer, improving the electronic and interfacial properties of this layer⁴⁵. One of the proposed dopants is niobium (Nb) to replace Sn ions in a SnO₂ transport layer. This dopant has proven to increase the fill factor by substantially decreasing the series resistance. In general,

the hysteresis behavior of the perovskite solar cell is improved due to a better flux and faster extraction of carriers inside the active perovskite layer. Finally, one of the most popular methods to improve the stability of the perovskite solar device is utilizing passivation. Passivation is the process in where a small coat or layer of metal oxide is deposited on top of the target layer to protect it from humidity and the environment. This has popularized passivation as it prevents ion migration at the interface between the active and the transport layers^{9,46}. This is usually achieved by thermal oxidation and prevents a change of the semiconductor optoelectronic properties. One of the disadvantages that it presents is that passivation does not smooth the surface of the layer. This means improving the grain size to reduce roughness and recombination is challenging. Still, ways of improving stability and strength against the environment is important.

A literature review has been presented to understand the results and achievements from the scientific community in the last years. Many approaches have been presented, and still the novelty of this topic gives perovskite solar cells many areas to be researched. This thesis will present a mixed cation, mixed halide perovskite solar device with a controlled temperature fabrication process. The device structure, its characterization methods and results will be further discussed in the following chapter.

Chapter 3: Model Methodology and Development

3.1: MIXED-CATION, MIXED-HALIDE, SnO₂-BASED PEROVSKITE DEVICE

The device structure presented in this thesis consists of a mixed-cation, mixed-halide, SnO₂-based perovskite device. The active perovskite layer is a mixture with controlled ratio of FA, Cs, I, and Br, resulting in the final compound, FA_xCs_(1-x)Pb(I_yBr_(1-y))₃. The final device structure, presented in a 3-D model in Figure 3.1, is built over a ~600 nm fluorine tin oxide (FTO) coated glass substrate from Sigma-Aldrich, ~7 Ω/sq, which works as the transparent conducting oxide and front contact. On top of the substrate, a ~41.2 nm layer of tin oxide as the electron transport layer is deposited, followed by a ~400 nm layer of the research group's recipe (FA_{0.8}Cs_{0.2}Pb(I_{0.86}Br_{0.14})₃) for the perovskite active layer. Then, ~315nm of SpiroOMeTAD (Sigma Aldrich) for the hole transport layer is deposited, and finally an 80 – 100 nm silver layer is thermally evaporated to deposit the reflective back contact. This structure is in a n-i-p configuration. Where light comes through the front transparent contact, goes first through the ETL (n-layer), the absorber active layer (i-layer), the HTL (p-layer) and finally through the back contact. The optimization of the layer thicknesses and device fabrication was also investigated to improve its efficiency and stability. The device fabrication process will be presented in a subsequent section.

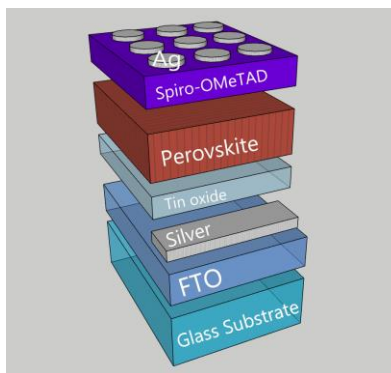


Figure 3.1: n-i-p device structure for perovskite solar cells.

3.2: DEVICE FABRICATION

The glass substrate was coated with fluorine tin oxide (FTO) on one side making it conductive, while the other side remains as a glass insulator. A multimeter was used to check continuity and identify the FTO coated side. A cleaning process is needed to remove any contaminants or particles presented on the surface of the substrate. The glass substrates were first gently brushed with deionized water to remove any major particles. Then, an ultrasonic cleaning was performed by placing the substrates in a petri dish filled with acetone to then be placed in the ultrasonic agitator for 2 min. This process was repeated two times by replacing the acetone with methanol and deionized water. The glass substrates were then dried with N_2 to remove any excess or chemical residual. This step is very important as the subsequent layers will be deposited and particles on the surface could affect its uniformity and the device operability.

As shown in the diagram previously presented, one must have access at the end, to both front and back contacts. An edge isolation must be performed on top of the FTO layer to be able to deposit the following layers without losing access to the front contact. This edge isolation was performed by placing a 1-inch width yellow tape on the top front of the surface, removing any air bubbles.

The electron transfer layer was done by spin coating 100 μ L of SnO_2 for 30 s at 3000 rpm. Immediately afterwards, the samples were placed on a hot plate for a soft bake at 100 $^{\circ}C$ for 10 min, and at 180 $^{\circ}C$ for 1 h for a hard bake to help crystallization and further elimination of residual solvents. The ETL deposition is a two-step deposition. A post-treatment chemical bath deposition (CBD) was performed as it aids to enhance the SnO_2 properties, such as conformality and blocking capabilities¹⁸. The samples were placed into another petri dish filled with SnO_2 solution previously stirred and covered to prevent evaporation of the SnO_2 . The dishes were then placed on

a hot plate at 70 °C for 3 h. Samples were then sonicated with DI water for 2 min to remove any excess SnO₂, and dried with N₂. A final annealing is performed at 180 °C for 1 h to complete the SnO₂ layer.

The perovskite active layer is deposited with a two-step spin coating process. 100 μL of FA_{0.8}CS_{0.2}Pb(I_{0.86}Br_{0.14})₃ (Perovskite A) was spin coated for 10 s at 1000 rpm for the first step, and for 20 s at 6000 rpm for the second step. In the last 10 s of the second step spin-coating 100 μL of chlorobenzene (CBZ) was deposited in the middle close to the surface²². CBZ is deposited as it has proven to be an antisolvent capable of increasing the perovskite grain size, which helps with carrier transport and uniformity⁴⁷. The sample was then annealed at 100 °C for 1 h.

The hole transport layer was created by spin coating 100 μL of Spiro-OMeTAD for 45 s at 2000 rpm. Then, the edge isolation tape was removed before depositing the final silver contact layer using the masking pattern shown in Fig. 3.2 below. Vapor deposition by thermal evaporation of Ag is performed to deposit the 80-100 nm silver contact layer.

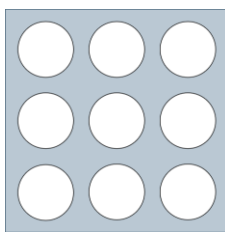


Figure 3.2: Masking pattern used for Ag evaporated back contacts.

Chapter 4: Results, Characterization, and Discussion

As mentioned before, there have been many approximations to improve the performance of perovskite solar cells and its stability. With the many options, there must also exist strong characterization methods that help research groups to visually understand the chemical properties, advantages, and disadvantages of the different recipes for the perovskite solar cell. This thesis will support its data by presenting XPS, PL, lifetime, SEM, AFM, J-V, and EQE. For the secondary grain growth, the perovskite will still remain the same, only additional measurements of SEM, J-V, and EQE will be presented.

4.1: X-RAY PHOTOELECTRON SPECTROSCOPY AND ULTRAVIOLET PHOTOELECTRON SPECTROSCOPY

XPS measurements were performed for two different recipes of the perovskite. Perovskite A ($\text{FA}_{0.8}\text{Cs}_{0.2}\text{Pb}(\text{I}_{0.86}\text{Br}_{0.14})_3$), which is the one used for the device fabrication and Perovskite B ($\text{FA}_{0.83}\text{Cs}_{0.17}\text{Pb}(\text{I}_{0.5}\text{Br}_{0.5})_3$). Perovskite B is used for comparison as it is a tuned higher band gap material which will be used for future research in tandem cells. These experiments were performed using an UHV-MultiProbe Surface Analysis System at Brookhaven National Laboratory with binding energies ranging 0 to 1100 eV, and probes with depths up to 10 nm. The XPS spectra for Perovskite A and Perovskite B are shown in Figure 4.1 and Figure 4.2 respectively, and the main information provided by XPS is chemical composition, in addition, an indication of degradation of material by oxidation.

Elements present in the material will be shown as peaks at its distinctive binding energies. For Perovskite A, the main peaks shown after 500 hours include cesium (Cs), iodine (I), oxygen (O), nitrogen (N), carbon (C), lead (Pb), and bromine (Br). By looking at the chemical composition of the perovskite recipe ($\text{FA}_{0.8}\text{Cs}_{0.2}\text{Pb}(\text{I}_{0.86}\text{Br}_{0.14})_3$), the peaks of cesium, lead, iodine, bromine,

carbon, and nitrogen are expected to appear in the spectra. The oxygen peak must be noticed appearing at its binding energy ~ 532 eV. This oxygen peak is caused by the oxidation due to the binding of lead, and hygroscopic nature of FA, which generate iodine (I_2), lead iodide (PbI_2), and lead oxides. Still, this oxygen peak is not noticeable as shown in its elemental concentration at a low 7.34 atomic % after 500 h. Other elemental concentrations presented include carbon at 75.38 atomic %, due to residues inside the XPS machine, lead with 8.20 atomic %, and iodine and bromine with a combined 8.06 atomic %. The last three give a ratio of $(I+Br)/Pb$ of 0.98. In general, the low oxygen peak after 500 h is a good indicator of the stability of the perovskite recipe against exposure and humidity as it is not oxidizing as fast as other materials in literature⁴⁸. For Perovskite B, the same peaks are expected, but with different peak amplitudes. Bromine shows a higher peak, while cesium decreases due to the ratio changes in the material, still the oxygen peak is almost negligible.

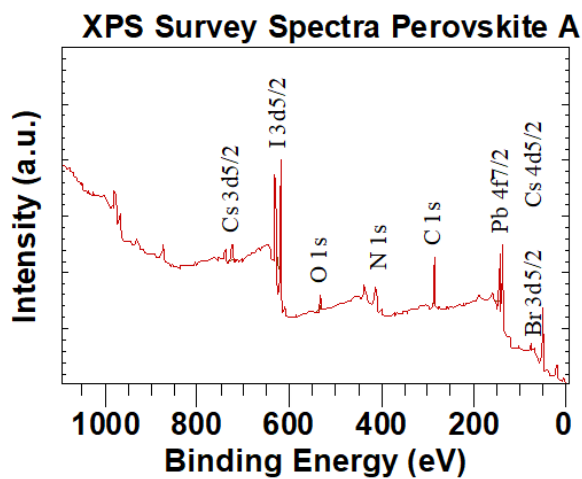


Figure 4.1: XPS survey spectra of the Perovskite A documented after 500 hours showing a small oxygen and lead peak, indicator of good stability.

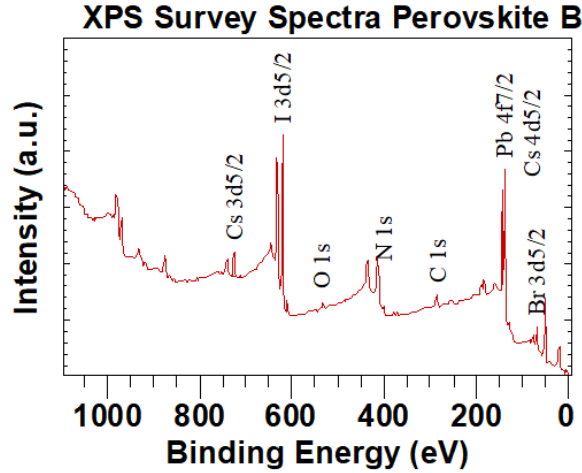


Figure 4.2: XPS survey spectra of the Perovskite B documented after 500 hours showing a big lead peak, indicator of lead migration due to oxidation of perovskite layer.

UPS spectra is also shown which is used to obtain the valence band energy and work function of the material. Both Perovskite A and Perovskite B spectra are shown in Figure 4.3. The valence band and work function of Perovskite A are ~ 0.9 eV and ~ 4.6 eV respectively, while Perovskite B shows a valence band of ~ 0.9 eV and ~ 4.5 eV. These results can be compared to values found in literature⁴⁸.

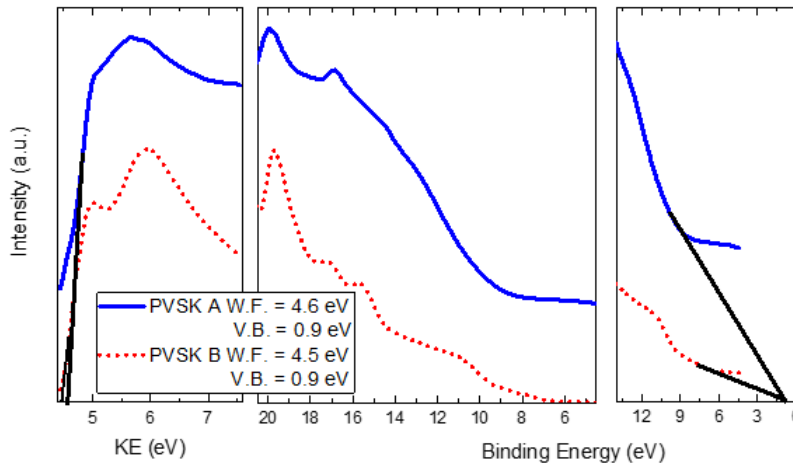


Figure 4.3: UPS spectra showing the work function and valence band for both Perovskite A and Perovskite B.

4.2 PHOTOLUMINESCENCE SPECTROSCOPY AND LIFETIME

Photoluminescence measurements provide information about bandgap and carrier lifetime of the material, which is a good indicator of the tuning capability of perovskite. These measurements were performed with the Olympus IX81 Confocal and the Picoquant devices. The data was analyzed and processed using the FluorEssence v.35 software. Perovskite A, which mixture is $\text{FA}_{0.8}\text{Cs}_{0.2}\text{Pb}(\text{I}_{0.86}\text{Br}_{0.14})_{0.3}$, shows an expected band gap of 1.6 eV, while Perovskite B $\text{FA}_{0.83}\text{Cs}_{0.17}\text{Pb}(\text{I}_{0.5}\text{Br}_{0.5})_{0.3}$ shows a higher band gap of 1.8 eV. Both PL spectra are shown in Figure 4.4. These band gaps are good indicators of the band gap tuning capabilities of perovskites by changing the ratios of the chemicals present in the mixture. In PL measurements the highest peak of the spectra corresponds to the photo-excitation process, which happens when the energy from the photon is high enough to make an electron jump from the valence band into the conduction band to then release energy to finally relax and return to the valence band. In other words, it gives the energy value of the band gap at which the perovskite will absorb light. Also, the band gap energy is inversely proportional to the wavelength of the light, as Perovskite A wavelength was found to be ~ 780 nm. This means a red shift, which is a transition to a higher wavelength and a lower band gap compared to Perovskite B (~ 715 nm and ~ 1.8 eV).

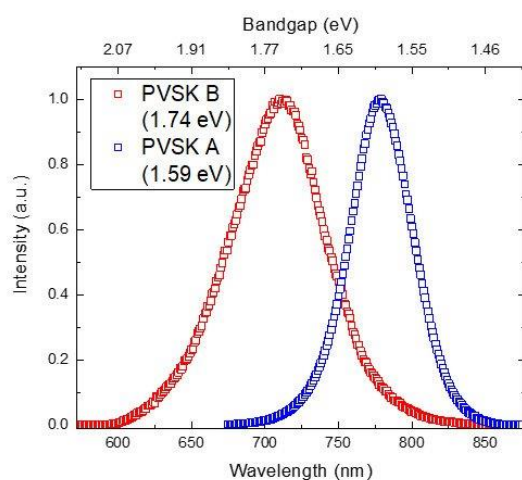


Figure 4.4: PL spectra showing a wavelength of 1.59 eV for Perovskite A and 1.74 eV for Perovskite B.

Photoluminescence measurements also provide important data regarding charge carrier lifetime. Carrier lifetime is crucial for the performance of the device as a higher lifetime increase the probability of the carrier to reach the contacts to be absorbed before recombination. Lifetime measurements were performed utilizing the PicoHarp 3000 Time-Correlated Single Photon Counting (TCSPC) system with 2.95 kV and a repetition rate ranging 1.0-7.94 MHz. The data was captured, processed, and fitted using the Fluofit software. With an excitation at 532 nm, Perovskite A lifetime was measured to be around ~ 274.69 ns while Perovskite B shows to be just ~ 17.99 ns. Both spectra are shown in Figure 4.5. As mentioned before, lifetime of carriers can be improved by having larger grain sizes while also eliminating as many traps possible at the surface. One approach to increasing carrier lifetime is to optimize the anneal times and temperatures, but with some tradeoffs that will be discussed in the SEM and AFM section.

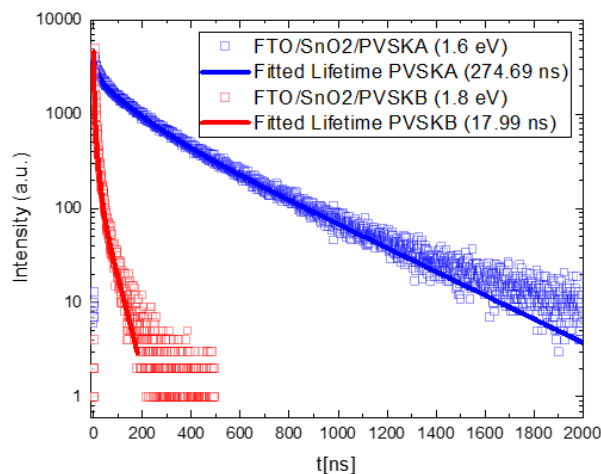


Figure 4.5: PL decay and lifetime for Perovskite A with a lifetime of 274.69 ns and Perovskite B with a lifetime of 17.99 ns.

4.3: SEM AND AFM

An SEM device is capable of providing cross section images of the complete device and surface images of the perovskite thin layer. The SEM images were produced using a Helios Nanolab (FEI) dual-beam system with high resolution SEM (1 nm). Figure 4.6 shows the cross section of the complete device in where all the layers can be seen with their respective thicknesses.

The device is fabricated on a glass substrate, shown in Figure 4.6. On top of the glass substrate, a ~600 nm FTO layer can be seen. This layer is the thickest one as it must be able to isolate the device from the glass substrate as glass is an insulator. It also works as the front contact, meaning it must be as stable as possible. This thickness is controlled by Sigma Aldrich, and the glass substrate arrives already coated with the FTO. The next layer seen is a thin (~41.2 nm in this device) SnO₂ layer which works as the electron transport layer. Controlling the thickness of this layer is important as it must be as thin as possible to have better energy level matching and reduce the resistance. The thickness was controlled by processing parameters including spin speed, and the CBD temperature and time, in addition to having an optimum temperature when annealing the layer. Still, peaks and valleys are seen in the SnO₂ layer due to imperfections, a non-uniform crystallization through the surface, and also the fact that being very thin makes it more prone to nonuniformity. The next layer is the active perovskite layer (~400 nm). This layer must be thick enough to work as a “rejection” layer between the ETL and the HTL. This means that electron hole pairs generated at the active layer will be separated and electron layers will go into the ETL and holes into the HTL. If it is not thick enough the electrons and holes could recombine inside the active layer without being able to be collected by their respective transport layers. A thick active perovskite layer has proven to be a main reason of V_{oc} increase⁴⁹. The hole transport layer (~314.8 nm Spiro-OMeTAD) is a thin layer that aids holes to reach the back-metal contact easier as it is a smaller distance between the active layer and the back contact. At the same time, this layer cannot be too thin due to the same reason as the ETL layer in where uniformity gets more difficult to achieve, reducing reproducibility. Finally, the silver contact layer (~82.3 nm) works as the back contact. This layer is thin to reduce resistance, but is the most uniform and stable due to its vapor deposition process. This layer could be replaced with gold to achieve better contact, more mobility, and less resistance overall.

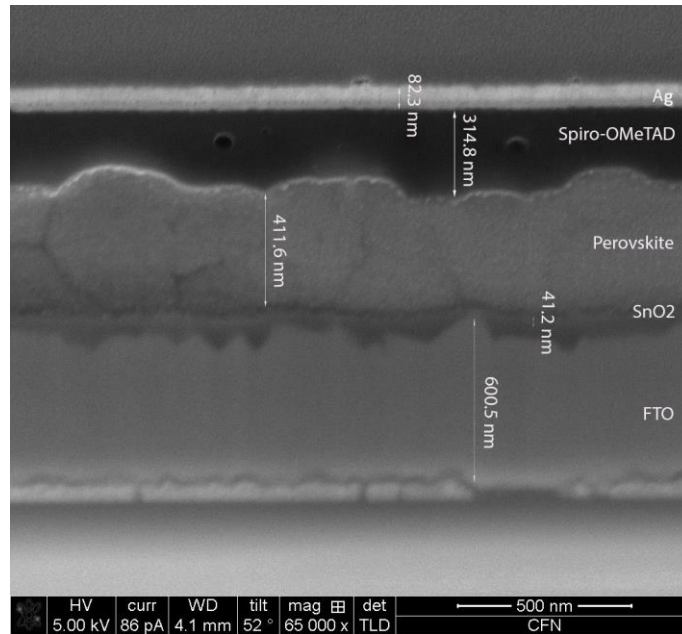


Figure 4.6: SEM of Perovskite A-based device showing a cross section of the layers in the device structure.

Improving the perovskite film’s grain size, boundaries, crystallization and its microstructure in general is the next step towards scalability. A bigger grain means an even surface and less defects that could cause local energy states inside the band gap, which eventually create recombination traps for the carriers, reducing the current⁴⁷. Figure 4.7 shows a top view SEM image of the perovskite film layer. As seen on the figure, there are several different grain sizes in the surface. The best-case scenario would be to be able to have a single grain or crystal. Still, the size of each crystal is above 100 nm, which still is a good grain size to achieve higher V_{oc} and efficiencies.

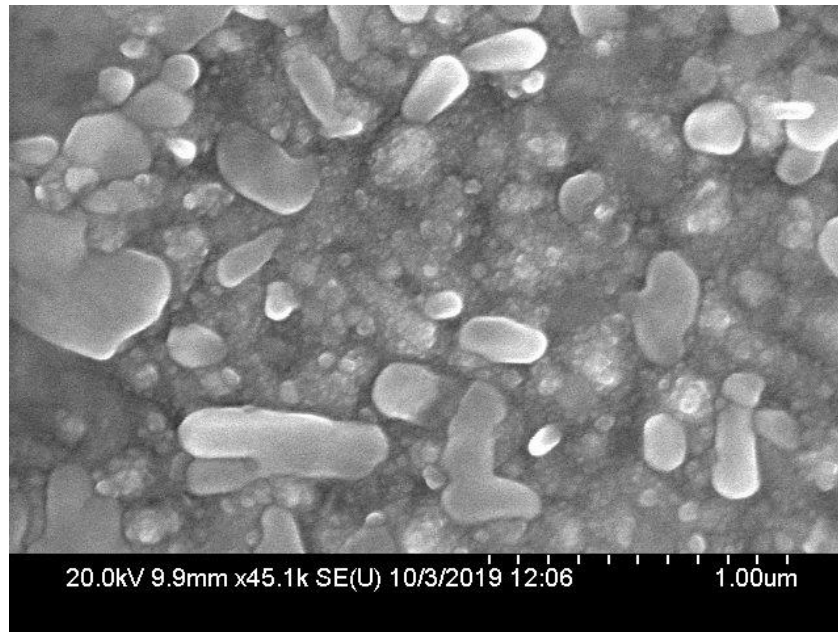


Figure 4.7: Top view SEM image of Perovskite A film showing the average crystal size close to 100 nm.

AFM is also a way to measure and visualize crystal grain size, thickness of a film, and roughness (uniformity). These measurements were performed for the Perovskite A layer at the Center of Nanofabrication Materials (CFN) at Brookhaven National Laboratory using the NX20 AFM device from Park Systems with a $10\ \mu\text{m} \times 10\ \mu\text{m}$ scanning area and the Smart Scan software for processing. Figure 4.8 shows a topography and a summary of the main properties of the surface of the perovskite film including grain statistics and surface roughness. The average grain size is shown to be $\sim 146\ \text{nm}$, corresponding to the top view presented before, and a roughness of $\sim 45.348\ \text{nm}$. Larger grains mean better mobility as it means less boundaries between crystals, giving more opportunity to carriers to reach the transport layers. Figure 4.9 shows a more precise thickness measurement of the perovskite layer. The $\sim 400\ \text{nm}$ perovskite layer shown in the figure approaches the optimum thickness ranging between $300\text{-}380\ \text{nm}$ from literature^{50,51}. Finally, the roughness can be seen in both figures in where the roughness should be controlled to prevent perforations of subsequent layers and contacts with the top layers. As discussed earlier, bigger grains reduce the grain boundaries, increasing roughness. Also, as discussed before, a secondary growth, or a secondary perovskite deposition could fill the spaces left from the grain boundaries and increase

the average grain size and roughness, reducing recombination. This will be discussed in the future work section.

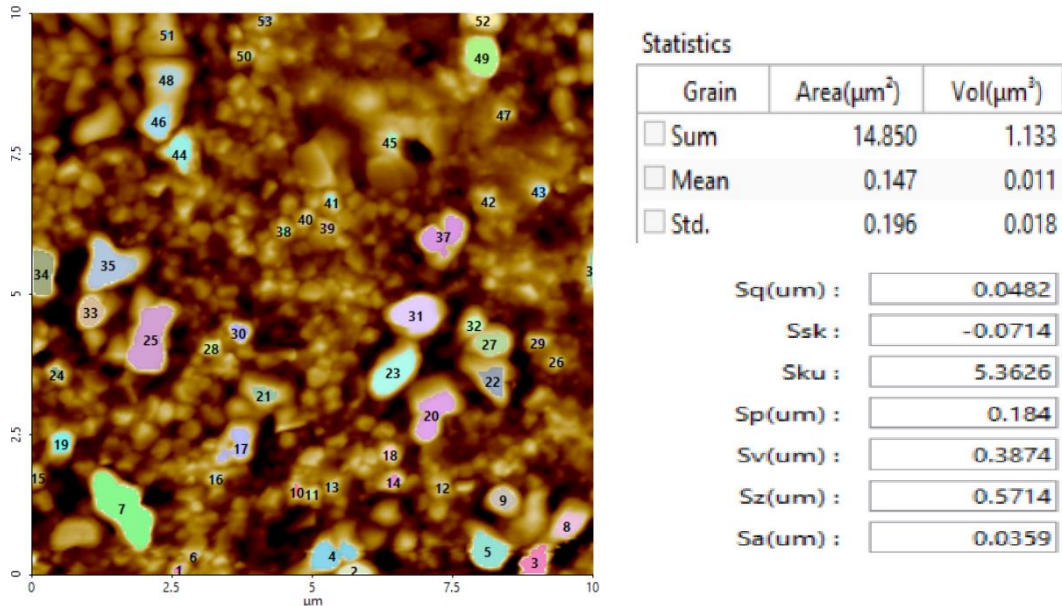


Figure 4.8: AFM measurement of Perovskite A showing the roughness and average grain size close to ~ 147 nm. This compares with the 100 nm shown in the SEM data.

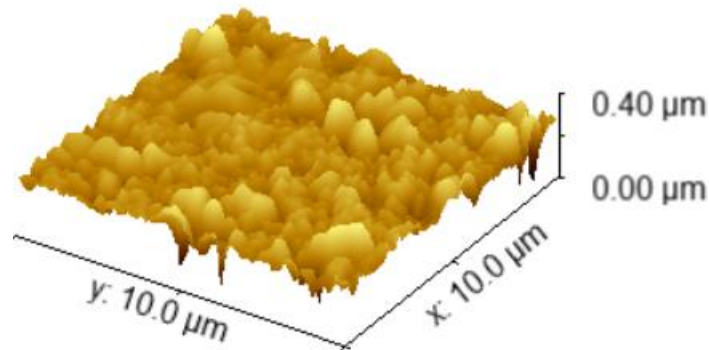


Figure 4.9: Thickness and topography of Perovskite A showing a thickness close to 400 nm.

4.4: J-V AND EQE MEASUREMENTS

After analyzing the structure, the device fabrication process, and an extensive characterization of the perovskite, three J-V measurements were taken for each device to analyze

the average electrical performance of the complete device with Perovskite A and also Perovskite B as the active absorber layer. The measurements were performed at the Thin Films Photovoltaic Lab utilizing a Class ABA solar simulator from PV Measurement Inc. with Air MASS 1.5 global filtering, a continuous 5 cm x 5 cm, a Keithley 2400 source meter, and I-V software. External quantum efficiency measurements were also taken. The J-V and EQE curves are shown in Figure 4.10 and Figure 4.11 respectively. These curves show the highest power conversion efficiency values for Perovskite A cells and the average value for all Perovskite B cells. The average of Perovskite B cells is only shown as it does not surpass 1% by design, making them almost negligible. Discussion of results will focus on Perovskite A devices. The goal of these measurements was to try and make the devices as stable as possible. As discussed before, the temperatures and the environment were strictly controlled. Temperatures were measured constantly using a temperature gun, doing any required adjustments. All cells were annealed for 60 min at a temperature of 100 °C. The efficiency achieved outstanding values ranging 14 – 17% with cell 2 and 7 achieving the highest efficiencies of 15.50% and 16.9% respectively. Efficiency is proportional to the short circuit current and the fill factor of the devices as shown in Equation (4.1). Cell 2 presented a $J_{sc} = 23.2 \text{ mA/cm}^2$, $V_{oc} = 1.095 \text{ V}$, and fill factor = 61.0%. Cell 7 presented a $J_{sc} = 21.297 \text{ mA/cm}^2$, $V_{oc} = 1.0569$, and fill factor = 74.99 %. The importance of the fill factor must be noticed. Even when Cell 2 presented a higher J_{sc} and V_{oc} than Cell 7, the efficiency is still higher in Cell 7. By definition the fill factor is the ratio of the maximum power from the device to the product of the measured I_{sc} and V_{oc} as seen in Equation (4.2). Cell 2 presented a maximum power $P_{max} = 1.52 \text{ mW}$, which is lower compared to the one presented by Cell 7, $P_{max} = 1.62 \text{ mW}$.

$$n = \frac{V_{oc} I_{sc} FF}{P_{in}} \quad \text{Equation (4.1)}$$

$$FF = \frac{V_{MP} I_{MP}}{V_{oc} I_{sc}} \quad \text{Equation (4.2)}$$

Also, the fill factor provides information of series and shunt resistances. Shunt resistances are usually created by defects in the surface. These resistances are created in parallel to the output of the solar devices, meaning that a low shunt resistance creates an alternate path for current, reducing the overall voltage of the device. Equation (4.3) shows the relationship between fill factor, shunt resistance and open-circuit voltage, where FF_{SH} is the fill factor affected by the shunt resistance r_{SH} , and FF_o is the fill factor not affected by the shunt resistance. Series resistance works in the opposite way. These resistances are created due to the resistance caused by the interface between the metal contacts and the absorber layer. The resistances are now in series to the output circuit and a higher series resistance reduces the fill factor as shown in Equation (4.4), where FF_s is the fill factor affected by the series resistance r_s . Cell 2 presents a lower shunt resistance (2000 Ω), and a higher resistance (106 Ω) compared to Cell 7 with a shunt resistance of 2950 Ω and a series resistance of 60.4 Ω . A summary of these results along the other cells with Perovskite A as their absorber layer are presented in Table 4.1.

$$FF_{SH} = FF_o \left(1 - \frac{V_{oc} + 0.7 FF_o}{V_{oc}} \frac{r_{SH}}{r_{SH}}\right) \quad \text{Equation (4.3)}$$

$$FF_s = FF_o (1 - r_s) \quad \text{Equation (4.4)}$$

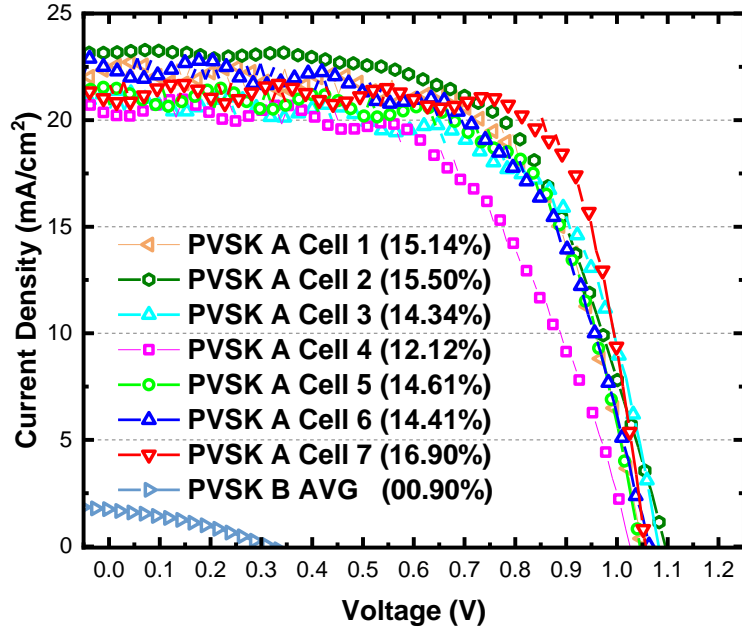


Figure 4.10: Perovskite A and Perovskite B J-V curves annealed at 100 °C for 1 hour.

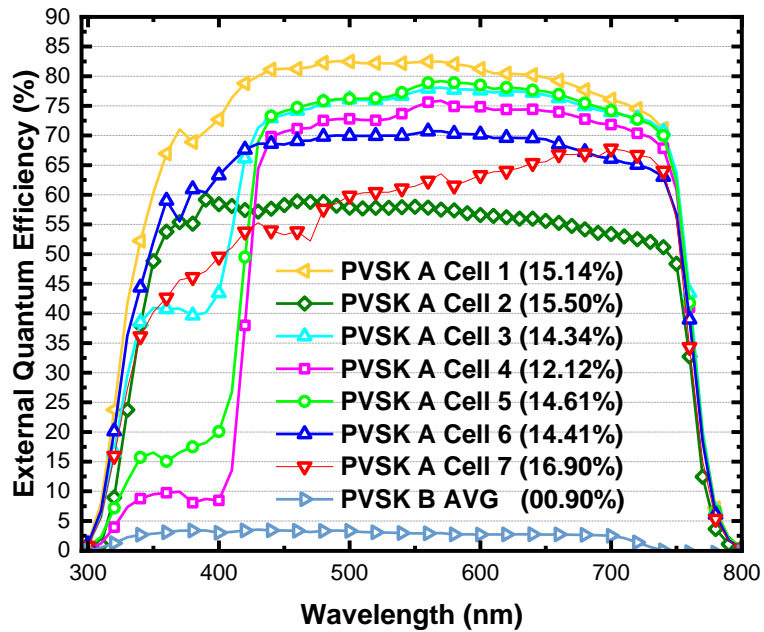


Figure 4.11: Perovskite A and Perovskite B EQE curves annealed at 100 °C for 1 hour.

Table 4.1: Summary of Results for Perovskite A cells

	$V_{oc}(V)$	$J_{sc}(mA/cm^2)$	$PCE(\%)$	$R_{SH}(\Omega \cdot cm^2)$	$R_s(\Omega \cdot cm^2)$	$FF(\%)$
1	1.049	22.3	15.1	1230	82.8	64.6
2	1.095	23.2	15.5	2000	106.0	61.0
3	1.082	20.7	14.3	857	75.0	63.7
4	1.025	20.5	12.1	224	100.0	57.4
5	1.045	21.0	14.6	3510	78.1	66.5
6	1.068	22.2	14.4	1250	88.8	62.6
7	1.056	21.2	16.9	2950	60.4	74.9

The External Quantum Efficiency, from Equation (4.5), measures the ratio of carriers collected to the number of photons at a given energy, illustrates an interesting behavior.

$$EQE = \frac{\text{Collected Charges at a Given Wavelength}}{\text{Photons in at a Given Wavelength}} \quad \text{Equation (4.5)}$$

$$= \frac{(current)/(charge\ of\ one\ electron)}{(total\ power\ of\ photons)/(energy\ of\ one\ photon)}$$

Cell 2 and Cell 7 with the highest efficiency present the lowest quantum efficiencies. This is caused by reflections in the cells. A coat of antireflective will be added in future experiments to improve EQE. Cell 1, 2, 3, 6, and 7 show a shape that shows a little of front surface recombination reflected in the blue response at lower wavelength and also back surface recombination reflected in the red response at higher wavelengths. Still work must be done to improve surface recombination, and still show a good performance. Cells 4 and 5 show a low blue response meaning there is more front surface recombination caused by the front contacts at the FTO interface. As discussed before, a high annealing time (1 hour) aids the crystallization process, improving the grain size of perovskite, reducing pinholes and recombination. Still, the temperature must not be higher 300 K as V_{oc} and J_{sc} tend to decrease due to the gaussian shape of trap states⁵². Also, it is important to notice how adding Cs and FA instead of MA improves performance by decreasing hysteresis, and series resistance⁵³.

Chapter 5: Future Work and Conclusion

5.1: FUTURE WORK ON GUANIDINIUM BROMIDE FOR SECONDARY GRAIN GROWTH

The power conversion efficiency of perovskite solar cells is currently limited by the relatively low open-circuit voltage (V_{oc}). In literature, most of the inverted perovskite solar cells present average V_{oc} values above 1.05 V. This is caused by, as mentioned before, non-radiative recombination losses and traps near the interface between the active perovskite layer and both back and front contacts^{54,55}. Reducing the nonradiative recombination is the next step to increase V_{oc} in PSCs. In a typical device structure, the active layer is deposited between an n-type layer (electron transport layer), and a p-type layer. Literature review has shown evidence that the nature and doping state of the active perovskite layer near the interface with both the ETL and HTL is influenced by the polarity of the substrate in where the active perovskite layer was deposited. For example, if the device is fabricated in a p-i-n configuration, in where the hole transport layer is first deposited on top of the front contact and the glass substrate, the perovskite layer will show a more p-type nature. On the other hand, in a n-i-p configuration, the active layer will show a more n-type nature as it is grown in top of the electron transport layer. In this thesis, the chosen configuration is the n-i-p. In this configuration, being more n-type, the traps causing the non-radiative recombination in the perovskite layer will be electron traps⁵⁶. This means that controlling the nature of the perovskite layer will help to increase its open-circuit voltage.

A research team from Peking University in Beijing along with other research teams from the University of Oxford, have presented a secondary grain growth technique capable of enhancing the open circuit voltage based on the information presented above⁵⁷. Their device structure is different to what is presented in this thesis, but still is a n-i-p configuration with a mixed-cation lead mixed-halide perovskite layer $(FA_{0.95}PbI_{2.95})_{0.85}(MAPbBr_3)_{0.15}$ ^{58,59}. After fabricating their device, they used scanning electron microscopy to analyze the surface and grains of their

perovskite layer. They concluded that the electron traps were caused mainly by an excess of lead halide crystals ($\text{PbI}_{1.50}\text{Br}_{0.50}$). Their solution was to do a secondary grain growth process using guanidinium bromide (abbreviated as SSG-G). The use of SSG-G reduces the nonradiative recombination due to three factors. First, the SSG-G film makes the perovskite film more n-type which means that the SSG-G grains will actually fill the electron traps discussed before, giving the opportunity to carriers to pass through into the transport layers. Second, an additional SSG-G film also produces a trap passivation process, which helps the perovskite to be more resistant and stable against oxidation and the environment. Finally, the SSG-G film has a wider band gap than the perovskite which reduces recombination by making pushing traps into the bulk of the perovskite layer and away from the interface with the transport layers. Figure 5.1 presented in D. Luo and research team's publication from Peking University and the University of Oxford⁵⁷, shows a top-view SEM of both the control film and the perovskite film with the SSG-G secondary growth. The bright sections are the $\text{PbI}_{1.50}\text{Br}_{0.50}$ grains causing the non-radiative recombination. In the SSG-G SEM the bright grains are digested by the guanidinium bromide, which makes the perovskite layer more n-type, and in theory, reduces recombination.

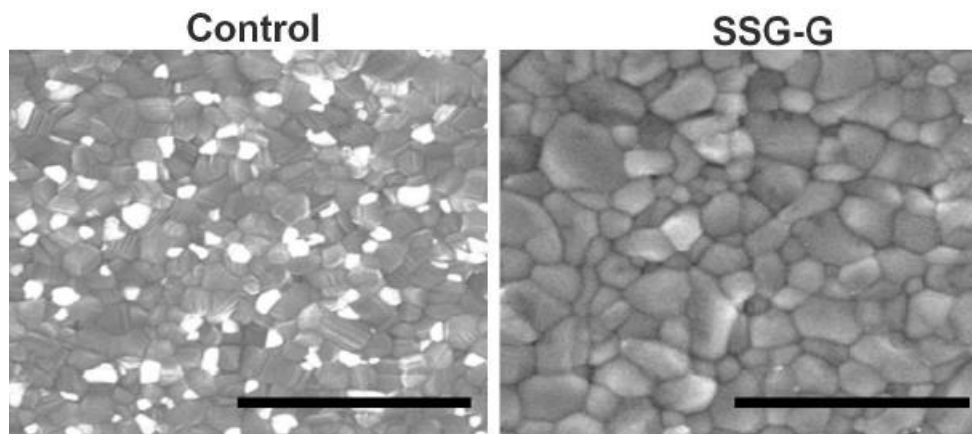


Figure 5.1 SEM images of the control and SSG-G films showing a reduction of $\text{PbI}_{1.50}\text{Br}_{0.50}$ grains due to the secondary grain growth.⁵⁷

5.2: CONCLUSION

This thesis has reported that a controlled-temperature improved manufacturing process has effectively increased the efficiency and overall performance of a single perovskite solar cell. These results are supported by a strong characterization of the device. The reported method utilizes $\text{FA}_{0.8}\text{Cs}_{0.2}\text{Pb}(\text{I}_{0.86}\text{Br}_{0.14})_{0.3}$ for the perovskite active layer. This mixed-cation, mixed-halide perovskite has increased the average open circuit voltage above 1.05 V and the short current density ranging between 20–23 mA/cm^2 . The absorption and band gap tuning capability were also enhanced. The ETL, HTL, and active layers were all temperature controlled to ensure a constant optimal carrier collection. In general, the power conversion efficiency improved to an average of 15%. Still, improvements will be done as this technology has the potential of achieving and surpassing 21% power conversion efficiency.

References

- [1] K. S. Hansen, R. J. Barthelmie, L. Jensen, and A. Sommer, “The impact of turbulence intensity and atmospheric stability on power deficits due to wind turbine wakes at horns rev wind farm,” *Wind Energy* 15, 183–196 (2012).
- [2] V. Andrei, K. Bethke, and K. Rademann, “Thermoelectricity in the context of renewable energy sources: joining forces instead of competing,” *Energy Environmental Science* 9, 1528–1532 (2016).
- [3] N. J. Jeon, H. Na, E. H. Jung, T. Yang, Y. G. Lee, G. Kim, H. Shin, S. I. Seok, J. Lee, and J. Seo, “A fluorene-terminated hole-transporting material for highly efficient and stable perovskite solar cells,” *Nature Energy* 3, 682–689 (2018).
- [4] I. Chakaberia, M. Cotlet, M. Fisher-Levine, D. R. Hodges, J. Nguyen, and A. Nomerotski, “Time stamping of single optical photons with 10 ns resolution,” *Advanced Photon Counting Techniques XI International Society for Optics and Photonics* 10212, 102120Q (2017).
- [5] S. Shahriar, C. Sana, J. Galindo, D. Kava, D. R. Hodges, E. Castro, R. Cotta, D. Buck, and L. Echegoyen, “Characterization and analysis of structural and optical properties of perovskite thin films,” *2015 IEEE 42nd Photovoltaic Specialist Conference (PVSC)*. IEEE, 1–6 (2015).
- [6] M. Gratzel, “The light and shade of perovskite solar cells”, *Nature Materials* 13, 838–842 (2014).
- [7] H. J. Snaith, “Perovskites: the emergence of a new era for low-cost, high efficiency solar cells,” *The Journal of Physical Chemistry Letters* 4, 3263–3630 (2013).
- [8] E. H. Jung, N. J. Jeon, E. Y. Park, C. S. Moon, T. J. Shin, T. Y. Yang, J. H. Noh, and J. Seo, “Efficient, stable and scalable perovskite solar cells using poly (3-hexylthiophene),” *Nature* 567, 511–515 (2019).
- [9] M. M. Tavakoli, M. Saliba, P. Yadav, P. Holzhey, A. Hagfeldt, S. M. Zakeeruddin, and M. Gratzel, “Synergistic crystal and interface engineering for efficient and stable perovskite photovoltaics,” *Advanced Energy Materials* 9, 1802646 (2019).
- [10] T. Sherahilo, “Oxford pv perovskite solar cell achieves 28% efficiency,” *Oxford PV* Retrieved from [https://www.oxfordpv.com/news/oxford-pvperovskite-solar-cell-achieves-28-efficiency\(2018\)](https://www.oxfordpv.com/news/oxford-pvperovskite-solar-cell-achieves-28-efficiency(2018)).
- [11] H. Imran, I. Durrani, M. Kamran, T. M. Abdolkader, M. Faryad, and N. Z. Butt, “High-performance bifacial perovskite/silicon double-tandem solar cell,” *IEEE Journal of Photovoltaics* 8, 1222–1229 (2018).
- [12] D. P. McMeekin, S. Mahesh, N. K. Noel, M. T. Klug, J. Lim, J. H. Warby, J. M. Ball, L. M. Herz, M. B. Johnston, and H. J. Snaith, “Solution-processed all-perovskite multi-junction solar cells,” *Joule* 3, 387–401 (2019).
- [13] P. K. Nayak, S. Mahesh, H. J. Snaith, and D. Cahen, “Photovoltaic solar cell technologies: analyzing the state of the art,” *Nature Reviews Materials* 4, 269–285 (2019).
- [14] D. Mitzi, “Introduction: Perovskites,” *Chemical Reviews* 119, 3033–3035 (2019).
- [15] Hardin, B. E., Snaith, H. J., & McGehee, M. D. (2012). The renaissance of dye-sensitized solar cells. *Nature photonics*, 6(3), 162.

- [16] Kojima, A., Teshima, K., Shirai, Y., & Miyasaka, T. (2009). Organometal halide perovskites as visible-light sensitizers for photovoltaic cells. *Journal of the American Chemical Society*, 131(17), 6050-6051.
- [17] Im, J. H., Lee, C. R., Lee, J. W., Park, S. W., & Park, N. G. (2011). 6.5% efficient perovskite quantum-dot-sensitized solar cell. *Nanoscale*, 3(10), 4088-4093.
- [18] Brown, I. D., & Poepelmeier, K. R. (Eds.). (2014). *Bond valences* (Vol. 158). Berlin (Heidelberg): Springer.
- [19] Xiang, H. J., Guennou, M., Íñiguez, J., Kreisel, J., & Bellaiche, L. (2017). Rules and mechanisms governing octahedral tilts in perovskites under pressure. *Physical Review B*, 96(5), 054102.
- [20] Butler, K. T. (2018). The chemical forces underlying octahedral tilting in halide perovskites. *Journal of Materials Chemistry C*, 6(44), 12045-12051.
- [21] G. Grancini and M. K. Nazeeruddin, "Dimensional tailoring of hybrid perovskite for photovoltaics," *Nature Reviews Materials* 4, 1 (2018).
- [22] E. H. Anaraki, A. Kermanpur, L. Steier, K. Domanski, T. Matsui, W. Tress, M. Saliba, A. Abate, M. Gratzel, A. Hagfeldt, and J. C. Baena, "Highly efficient and stable planar perovskite solar cells by solution-processed tin oxide," *Energy Environmental Science* 9, 3128–3134 (2016).
- [23] Tzounis, L., Stergiopoulos, T., Zachariadis, A., Gravalidis, C., Laskarakis, A., & Logothetidis, S. (2017). Perovskite solar cells from small scale spin coating process towards roll-to-roll printing: optical and morphological studies. *Materials Today: Proceedings*, 4(4), 5082-5089.
- [24] Lokhande, C. D. (1991). Chemical deposition of metal chalcogenide thin films. *Materials Chemistry and Physics*, 27(1), 1-43.
- [25] Mattox, D. M. (2010). *Handbook of physical vapor deposition (PVD) processing*. William Andrew.
- [26] Z. Ahmad, M. A. Najeeb, R. A. Shakoor, A. Alashraf, S. A. Al-Muhtaseb, A. Soliman, and M. K. Nazeeruddin, "Instability in $\text{CH}_3\text{NH}_3\text{PbI}_3$ perovskite solar cells due to elemental migration and chemical composition changes," *Scientific reports* 7, 15406 (2017).
- [27] V. Kheraj, B. J. Simonds, A. Toshniwal, S. Misra, P. Peroncik, C. Zhang, Z. V. Vardeny, and M. A. Scarpulla, "Using photoluminescence to monitor the optoelectronic properties of methylammonium lead halide perovskite in light and dark over periods of days," *Journal of Luminescence* 194, 353–358 (2018).
- [28] B. Conings, J. Drijkoningen, N. Gauquelin, A. Babayigit, J. D'Haen, L. D'Olieslaeger, A. Ethirajan, J. Verbeeck, J. Manca, E. Mosconi, F. D. Angelis, and H. Boyen, "Intrinsic thermal instability of methylammonium lead trihalide perovskite," *Advanced Science* 5, 1500477 (2015).
- [29] D. McMeekin, G. Sadoughi, W. Rehman, G. Eperon, M. Saliba, M. Horantner, A. Haghighirad, N. Sakai, L. Korte, B. Rech, M. B. Johnston, L. Herz, and H. J. Snaith, "A mixed-cation lead mixed-halide perovskite absorber for tandem solar cells," *Science* 351, 151–155 (2016).
- [30] M. Saliba, T. Matsui, J. Seo, K. Domanski, J. Correa-Baena, M. K. Nazeeruddin, S. M. Zakeeruddin, W. Tress, A. Abate, A. Hagfeldt, and M. Gratzel, "Cesium-containing triple cation perovskite solar cells: improved stability, reproducibility and high efficiency," *Energy Environmental Science* 9, 1853–2160 (2016).

- [31] C. Yi, J. Luo, S. Meloni, A. Boziki, A. Astani, C. Gratzel, S. Zakeeruddin, U. Rothlisberger, and M. Gratzel, "Entropic stabilization of mixed a-cation abx₃ metal halide perovskite for high performance perovskite solar cells," *Energy Environmental Science* 9, 656–662 (2016).
- [32] B. Conings, J. Drijkoningen, N. Gauquelin, A. Babayigit, J. D'Haen, L. D'Olieslaeger, A. Ethirajan, J. Verbeeck, J. Manca, E. Mosconi, F. D. Angelis, and H. Boyen, "Intrinsic thermal instability of methylammonium lead trihalide perovskite," *Advanced Science* 5, 1500477 (2015).
- [33] D. McMeekin, G. Sadoughi, W. Rehman, G. Eperon, M. Saliba, M. Horantner, A. Haghighirad, N. Sakai, L. Korte, B. Rech, M. B. Johnston, L. Herz, and H. J. Snaith, "A mixed-cation lead mixed-halide perovskite absorber for tandem solar cells," *Science* 351, 151–155 (2016).
- [34] J. Lee, D. Kim, H. Kim, S. Seo, S. M. Cho, and N. Park, "Formamidinium and cesium hybridization for photo- and moisture-stable perovskite solar cell," *Advanced Energy Materials* 5, 1501310 (2015).
- [35] H. Zarick, N. Soetan, W. Erwin, and R. Bardhan, "Mixed halide hybrid perovskites: a paradigm shift in photovoltaics," *Journal of Materials Chemistry A* 6, 5507–5537 (2018).
- [36] T. Jacobsson, S. Svanstrom, V. Andrei, J. Rivett, N. Kornienko, B. Philippe, U. Cappel, H. Rensmo, F. Deschler, and G. Boschloo, "Extending the compositional space of mixed lead halide perovskites by cs, rb, k, and na doping," *The Journal of Physical Chemistry C* 122, 13548–13557 (2018).
- [37] Kulkarni, S. A., Baikie, T., Boix, P. P., Yantara, N., Mathews, N., & Mhaisalkar, S. (2014). Band-gap tuning of lead halide perovskites using a sequential deposition process. *Journal of Materials Chemistry A*, 2(24), 9221-9225.
- [38] Unger, E. L., Kegelman, L., Suchan, K., Sörell, D., Korte, L., & Albrecht, S. (2017). Roadmap and roadblocks for the band gap tunability of metal halide perovskites. *Journal of Materials Chemistry A*, 5(23), 11401-11409.
- [39] I. Braly, R. Stoddard, A. Rajagopal, A. Uhl, J. Katahara, A. Jen, and H. Hillhouse, "Current-induced phase segregation in mixed halide hybrid perovskites and its impact on two-terminal tandem solar cell design," *ACS Energy Letters* 2, 1841–1847 (2017).
- [40] A. M. Zeidell, C. Tyznik, L. Jennings, C. Zhang, H. Lee, M. Guthold, Z. V. Vardeny, and O. D. Jurchescu, "Enhanced charge transport in hybrid perovskite field-effect transistors via microstructure control," *Advanced Electronic*, 1800316 (2018).
- [41] M. Singh, A. Ng, Z. Ren, H. Hu, H. Lin, C. Chu, and G. Li, "Facile synthesis of composite tin oxide nanostructures for high-performance planar perovskite solar cells," *Nano Energy* 60, 275–284 (2019).
- [42] A. Ghosh, S. Safat, and M. S. Islam, "Stable and efficient perovskite solar cell with metal oxide transport layers," 2019 International Conference on Electrical, Computer and Communication Engineering (ECCE), 1–5 (2019).
- [43] Q. Jang, X. Zhang, and J. You, "SnO₂: a wonderful electron transport layer for perovskite solar cells," *Small* 14, 1801154 (2018).
- [44] J. You, L. Meng, T. Song, T. Guo, Y. Yang, W. Chang, Z. Hong, H. Chen, H. Zhou, Q. Chen, Y. Liu, N. D. Marco, and Y. Yang, "Improved air stability of perovskite solar cells via solution-processed metal oxide transport layers," *Nature Nanotechnology* 11, 75–81 (2016).

- [45] E.H.Anaraki,A.Kermanpur,M.T.Mayer,L.Steier,T.Ahmed,S.Turren Cruz, J. Seo, J. Luo, S. M. Zakeeruddin, W. R. Tress, T. Edvinsson, M. Gratzel, A. Hagfeldt, and J. Correa-Baena, “Low-temperature nb-doped sno₂ electron-selective contact yields over 20% efficiency in planar perovskite solar cells,” *ACS Energy Letters*3, 773–778 (2018).
- [46] H. J. Snaith, “Present status and future prospects of perovskite photovoltaics,” *Nature Materials*17, 372–376 (2018).
- [47] S. Agarwal and P. R. Nair, “Performance optimization for perovskite based solar cells,” *IEEE Xplore*40(2014).
- [48] A. Calloni, A. Abate, G. Bussetti, G. Berti, R. Yivlialin, F. Ciccacci, and L. Duo, “Stability of organic cations in solution-processed ch₃nh₃pbi₃ perovskites: Formation of modified surface layers,” *The Journal of Physical Chemistry*119, 21329–21335 (2015).
- [49] W. Tress, M. Yavari, K. Domanski, P. Yadav, B. Niesen, J. P. Correa Baena, A. Hagfeldt, and M. Gratzel, “Interpretation and evolution of open circuit voltage, recombination, ideality factor and subgap defect states during reversible light-soaking and irreversible degradation of perovskite solar cells,” *Energy Environmental Science*11, 715 (2018).
- [50] R. Schmager, G. Gomard, B. Richards, and U. Paetzold, “Nanophotonic perovskite layers for enhanced current generation and mitigation of lead in perovskite solar cells,” *Solar Energy Materials and Solar Cells* 192, 65–71 (2019).
- [51] L. Phillips, A. Rashed, R. Trehame, J. Kay, P. Yates, I. Mitrovic, A. Weerakkody, S. Hall, and K. Durose, “Maximizing the optical performance of ch₃nh₃pbi₃ hybrid perovskite heterojunction stacks,” *ELSEVIER* 147, 327–333 (2016).
- [52] H. Lee, P. Tyagi, S. Rhee, M. Park, J. Song, J. Kim, and C. Lee, “Analysis of photovoltaic properties of a perovskite solar cell: Impact of recombination, space charge, exciton, and disorder,” *IEEE Journal of Photovoltaics*7, 1681–1686 (2017).
- [53] D. Prochowicz, M. M. Tavakoli, A. Solanki, T. W. Goh, T. C. Sum, and P. Yadav, “Correlation of recombination and open circuit voltage in planar heterojunction perovskite solar cells,” *Journal of Materials Chemistry C* 7, 1273–1279 (2019).
- [54] Ling, L., Yuan, S., Wang, P., Zhang, H., Tu, L., Wang, J., ... & Zheng, L. (2016). Precisely controlled hydration water for performance improvement of organic–inorganic perovskite solar cells. *Advanced Functional Materials*, 26(28), 5028-5034.
- [55] Huang, J., Yuan, Y., Shao, Y., & Yan, Y. (2017). Understanding the physical properties of hybrid perovskites for photovoltaic applications. *Nature Reviews Materials*, 2(7), 1-19.
- [56] Stranks, S. D., Burlakov, V. M., Leijtens, T., Ball, J. M., Goriely, A., & Snaith, H. J. (2014). Recombination kinetics in organic-inorganic perovskites: excitons, free charge, and subgap states. *Physical Review Applied*, 2(3), 034007.
- [57] Luo, D., Yang, W., Wang, Z., Sadhanala, A., Hu, Q., Su, R., ... & Liu, T. (2018). Enhanced photovoltage for inverted planar heterojunction perovskite solar cells. *Science*, 360(6396), 1442-1446.
- [58] Bi, D., Tress, W., Dar, M. I., Gao, P., Luo, J., Renevier, C., ... & Decoppet, J. D. (2016). Efficient luminescent solar cells based on tailored mixed-cation perovskites. *Science advances*, 2(1), e1501170.
- [59] Kim, Y. C., Jeon, N. J., Noh, J. H., Yang, W. S., Seo, J., Yun, J. S., ... & Ahn, T. K. (2016). Beneficial effects of PbI₂ incorporated in organo-lead halide perovskite solar cells. *Advanced Energy Materials*, 6(4), 1502104.

Vita

Luis Eduardo Valerio Frias, was born in Ciudad Juarez, Chihuahua. He graduated from Instituto Iberoamericano San Patricio High School in May 2014 and enrolled into The University of Texas at El Paso in August 2014. In May 2018, he was awarded with a B.S. in Electrical and Computer Engineering as a Summa Cum Laude. He started his M.S. in Electrical Engineering at The University of Texas at El Paso where he also became the president of Tau Beta Pi, the engineering honor society. He has interned at the University of Mayaguez, Puerto Rico, Brookhaven National Laboratory, and participated in the Hands-On Photovoltaic Experience workshop at the National Renewable Energy Laboratory. He published his first paper “Characterization and analysis of $\text{FA}_x\text{Cs}_{(1-x)}\text{Pb}(\text{I}_y\text{Br}_{(1-y)})_3$ perovskite solar cells with thickness-controlled transport layers for performance optimization” in the Journal of Applied Physics, and has presented at the IEEE PVSC conference, IXS, the U.S. Department of Education and other local conferences. He will start working at Intel Corporation later this year.

Contact Information: levaleriofrias@miners.utep.edu

(915)-259-4263